**THE EUROPEAN
PHYSICAL JOURNAL B**

Regular Article - Computational Methods

Dependence of cuprous oxide conductivity on metal doping: a hybrid density functional simulation

Mohammed Benaissa[a] , Hayet Si Abdelkader, and Ghouti Merad

Laboratory of Materials Discovery, Unit of Research Materials and Renewable Energies, LEPM-URMER,
University of Tlemcen, Tlemcen, Algeria

Abstract. Multiple metallic elements were screened as doping agents to alternate conductivity in cuprous oxide (Cu_2O). Energetic, charge transition levels and optical properties of Be, Mg, Ca, Sr, Zn, Cd, Hg, Al, Ga, and In substitutionally doped Cu_2O systems were investigated based on first principles methods. Results of formation energy calculation under both Cu-rich and Cu-poor conditions indicate the easy incorporation of 2A (Be, Mg, Ca, and Sr) group impurities into the crystal lattice of Cu_2O under both conditions. However, 3A (Al, Ga, and In) group impurities could be incorporated only under Cu-poor conditions. While, the incorporation of Zn, Cd, and Hg in Cu_2O is energetically less favorable under both conditions. The calculated charge transition levels of these dopants revealed an n-type conductivity. The calculated work functions show n-type to p-type surface inversion behavior for some doped systems. This can explain the p-type conductivity of Mg-doped Cu_2O found experimentally. Furthermore, the optical properties of each system are calculated to investigate the effect of the introduced impurity on Cu_2O. This study can help identify potential dopants to use for solar cell fabrication.

1 Introduction

Due to the increasing energy crisis and environmental issues, a transition to safer and renewable forms of energy resources is becoming increasingly urgent. It is obvious that the most common energy resource is solar radiation. Therefore, it is important to establish technologies to efficiently extract solar energy to the point that it becomes competitive with fossil fuels. Crystalline silicone technologies dominate most of the solar cell industry, providing good performance with relatively moderate-cost manufacturing methods [1]. However, silicon photovoltaic has reached a plateau in performance enhancement [1, 2] (efficiency vs manufacturing cost) due to the high-cost of higher purity single crystal silicon. Therefore, more attention is needed to find alternative materials.

Metal oxides represent a very intriguing class of semiconductors; widely known for their vast range of technological applications; particularly in the field of transparent conductors, optical smart windows, solar cells, and gas-sensors [3–8]. In the field of low-cost solar cells [9–12], cuprous oxide (Cu_2O) as one of many important metal oxide compounds is extensively investigated because of its good properties; possessing a very high absorption coefficient with direct band gap

ranging from 2 to 2.5 eV [12], non-toxic, abundant source materials and easy-to-scale manufacturing methods [10, 11]. To construct p–n homojunction for Cu_2O-based thin-film solar cells with improved conversion efficiency, the fabrication of high-conductivity n-type Cu_2O is extremely important and has been seen as a challenge for Cu_2O-based photovoltaics. Nowadays, very limited n-type dopants have been identified for Cu_2O. The experiment showed a reduced resistivity of Cl-doped Cu_2O by 5 orders of magnitude [10]. In-doped Cu_2O thin films were deposited using direct current magnetron co-sputtering showing n-type conductivity at room temperature [13]. Zn-doped Cu_2O have been prepared via single-step electrodeposition [14], they found that zinc doping increased the Fermi level relative to Cu_2O and enabled facile charge carrier injection/extraction with p-type Cu_2O. Homojunction solar cells were also fabricated, McShane et al. reported on the fabrication of a solar cell with an efficiency of up to 1.06% based on intrinsic doped Cu_2O homojunction [15]. Homojunction Cu_2O solar cells were fabricated with consecutive electrochemical depositions of a p-Cu_2O and an n-Cu_2O layer with the performance of up to 0.42% [16].

Some theoretical studies were also performed, Sieberer et al. examined the effect of substituting Cu by Mn, Fe, Co, and Ni in Cu_2O to explore its suitable semiconductor hosts properties for diluted magnetic

[a] e-mail: mohammed.benaissa@univ-tlemcen.dz (corresponding author)

semiconductors [17]. Another theoretical work also confirmed the n-type conductivity of Cu_2O with the incorporation of Indium; it is based on the reduction of the work function and the raise of the Fermi energy level of the doped system [13]. In our recent work [18], we predicted n-type conduction behavior among halogen dopants (F, Cl, Br) substituting O ions.

The objective of this study is to find new dopants ions to achieve n-type conductivity in Cu_2O. We also examined the effects of the different dopants on the formation energies, work function, electronic structure and optical properties of Cu_2O. Substitutional n-type doping in Cu_2O can be incorporated into either Cu or O sites. Based on the valence of Cu in Cu_2O (+ 1), we Choose Cu for the doping site. Total of 10 dopants including 2A (Be, Mg, Ca, Sr), 12B (Zn, Cd, Hg), and 3A (Al, Ga, In) group elements were chosen as possible donor impurity to achieve n-type conductivity.

2 Method of calculation

Energetic, work functions, electronic structure and optical properties simulations have been conducted using the projector augmented wave approach to describe the electron–ion interactions [19] and the screened hybrid functional as proposed by Heyd, Scuseria, and Ernzerhof (HSE) [20] within the density functional theory [21, 22]. Similar to Scalon et al. [23] the value of the exact nonlocal exchange α was set to 27.5%, which yielded a band gap of 2.04 eV for Cu_2O, in excellent agreement with the experimentally measured band gap (2.1 eV [12]). The calculation was done using the Vienna Abinitio Simulation Package (VASP) [24, 25]. The valence electron configurations used in these calculations are presented in Table 1.

Table 1 Valence electrons, Ionic radius and electronegativity of Cu, O, and M (Be, Mg, Ca, Sr, Zn, Cd, Hg, Al, Ga, In) ions

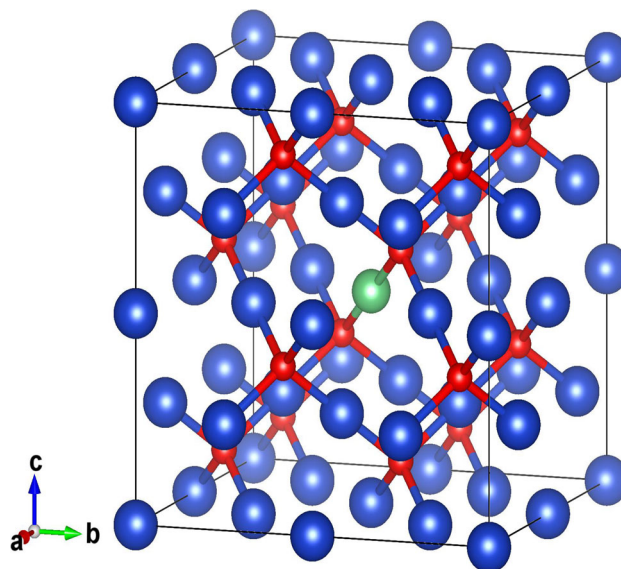| Ion	Valence	Ionic radius Å	Electronegativity
Cu	$4s^1\ 3d^{10}$	0.91	1.90
O	$2s^2\ 2p^4$	1.26	3.44
Be	$2s^2$	0.59	1.57
Mg	$3s^2$	0.86	1.31
Ca	$3p^6\ 4s^2$	1.14	1.00
Sr	$4s^2\ 4p^6\ 5s^2$	1.32	0.95
Zn	$4s^2\ 3d^{10}$	0.88	1.65
Cd	$5s^2\ 4d^{10}$	1.09	1.69
Hg	$6s^2\ 5d^{10}$	1.16	2.00
Al	$3s^2\ 3p^1$	0.68	1.61
Ga	$4s^2\ 4p^1$	0.76	1.81
In	$5s^2\ 5p^1$	0.94	1.78

Fig. 1 $2 \times 2 \times 2$ supercell of M-doped Cu_2O. Blue, red and green spheres represent Cu, O, and M (Be, Mg, Ca, Sr, Zn, Cd, Hg, Al, Ga, In) ions, respectively

The supercell used to model Cu_2O doped systems is described by a supercell containing 4-unit cells corresponding to a $2 \times 2 \times 2$ supercell containing 48 atoms. For surface supercell used to calculate the work function, we took the relaxed doping supercell structure and added a vacuum height of 12 Å to prevent the interactions between the slabs and their periodic images. After the incorporation of the impurity in the supercell, we run a structural optimization with the integration over the first Brillouin zone made using $4 \times 4 \times 4$ and $4 \times 4 \times 1$ Gamma-centered k-points grid generated according to the Monkhorst–Pack scheme [26] for the doping and surface supercells, respectively. The cut-off energy restricting the number of plane waves in the basis-set was fixed at 520 eV. The convergence criteria of both the total energy and ionic force were set to 0.1 meV and 1 meV/Å^3, respectively; allowing all structures to relax according to the Hellman–Feynman forces using the conjugate gradient algorithm.

3 Results and discussions

3.1 Structural and energetic properties

The Cu_2O crystal has a high symmetry cubic structure with $Pn\bar{3}m$ space group, where oxygen atoms are surrounded by four copper atoms in a tetrahedral configuration. The calculated lattice constant 'a' of Cu_2O is 4.315 Å, in line with the experimental results (a = 4.27 Å [27]). For the M-doped Cu_2O, the central copper atom was substituted by one dopant atom. The doping concentration is about 3.12%, which is comparable to experimental concentrations [13, 14]. The supercell model is illustrated in Fig. 1. As a first step, the dop-

Table 2 Crystal structures parameters and the average bond lengths of M-doped Cu_2O systems

System	a (Å)	Δa (%)	M–O (Å)	ΔM–O (%)
Cu_2O:Be	4.309	− 0.13	1.498	− 19.82
Cu_2O:Mg	4.335	0.48	1.927	3.14
Exp.[a]	4.2572			
Cu_2O:Ca	4.355	0.93	2.192	17.33
Cu_2O:Sr	4.368	1.23	2.339	25.20
Exp.[b]	4.2869			
Cu_2O:Zn	4.332	0.42	1.923	2.93
Cu_2O:Cd	4.350	0.81	2.208	18.19
Cu_2O:Hg	4.352	0.87	2.353	25.95
Cu_2O:Al	4.332	0.40	1.836	− 1.73
Cu_2O:Ga	4.337	0.52	2.129	13.96
Cu_2O:In	4.355	0.94	2.321	24.23
Exp.[c]	4.25–4.27			

[a]Ref. [29]
[b]Ref. [30]
[c]Ref. [13]

ing effects on the crystal structure of Cu_2O were analyzed using the calculated lattice parameters, listed in Table 2. The crystal distortion resulted from doping is very small for most of the systems, suggesting that this system could still keep the Cu_2O original crystal structure. Be dopant have compression effects on the system, reducing the lattice parameter 'a' by 0.13%, in agreement with its small ionic radius and high electronegativity compared to Cu (see Table 1). While, the rest of the dopants Mg, Ca, Sr, Zn, Cd, Hg, Al, Ga, In have expansion effects, with increasing of 'a' by 0.48% and 0.93%, 1.23%, 0.42%, 0.81%, 0.87%, 0.45%, 0.52%, and 0.94%, respectively; in correlation with their ionic radius.

A second important parameter is the M–O bond length (see Table 2). The relaxed Cu–O bond length of Cu_2O is 1.868 Å, which is in good agreement with the experimental results (1.84 Å) [28]. The effect on the M–O bond length is very noticeable. Be–O, and Al-O bond lengths are compressed with respect to the Cu–O one, while, the rest of dopants bond lengths are expanded (see Table 2). Mg–O, Zn–O, and Al–O bond lengths have shown negligible change due to the similarity in ionic radius between these dopants and Cu (see Table 1). We note that the experimental works also found a negligible structural change in In-, Zn-, Mg- and Sr-doped Cu_2O [13, 14, 29, 30].

To predict the relative stability of the pure and doped systems under both Cu-rich and Cu-poor growth conditions, formation energies of pure and M-doped Cu_2O were considered. The corresponding energies were calculated according to the following formulas [31, 32]:

$$\Delta E_{form}^{Cu_2O} = E_{Cu_2O} - (2\mu_{Cu} + \mu_O) \quad (1)$$

$$\Delta E_{form} = E_{Cu_2O:M} - E_{Cu_2O} - (n_M\mu_M - n_{Cu}\mu_{Cu}) \quad (2)$$

where E_{Cu_2O} and $E_{Cu_2O:M}$ correspond to the total energies of pure and M-doped Cu_2O supercell, respectively. μ_{Cu}, μ_O and μ_M are the chemical potentials of Cu, O, and M=Be, Mg, Ca, Sr, Zn, Cd, Hg, Al, Ga, In elements, respectively. n_{Cu} and n_M represent the number of Cu atoms removed, and M atoms added to the pristine Cu_2O supercell, respectively.

The chemical potentials of Cu and O are constrained by the relationships $\Delta E_{form}^{Cu_2O} = 2\Delta\mu_{Cu} + \Delta\mu_O$ and $\Delta E_{form}^{CuO} = \Delta\mu_{Cu} + \Delta\mu_O$. The calculated formation energy of pure Cu_2O and CuO are − 0.685 eV/atom and − 0.650 eV/atom, respectively, in reasonable agreement with the theoretical values of Isseroff et al. [33] of − 0.541 eV/atom and − 0.719 eV/atom. Under Cu-rich growth condition, the μ_{Cu} is taken as the energy of metallic Cu $\mu_{Cu}^{metallic}$. While, under the Cu-poor growth condition, μ_{Cu} is therefore taken as $\mu_{Cu} = \left(\Delta E_{form}^{Cu_2O} - \Delta E_{form}^{CuO}\right) + \mu_{Cu}^{metallic}$ [33]. The μ_M of the dopants species is taken as the calculated energy per atom of their stable solid-state primitive cell.

Table 3 resumes the impurity formation energy per atom of the M-doped Cu_2O systems under both Cu-rich and Cu-poor conditions. It indicates a clear trend where 2A group (Be, Mg, Ca, Sr) impurities could be readily incorporated into the crystal lattice of Cu_2O under both conditions. While, the incorporation of Zn, Cd and Hg, is energetically unfavorable due to their positive formation energy. Meanwhile, 3A group (Al, Ga, In) impurities could be readily incorporated into the crystal lattice of Cu_2O under Cu-poor conditions. We should note that In-, Mg- and Sr-doped Cu_2O are already fabricated experimentally [13, 29, 30], which is in very good agreement with our calculated formation energies. Meanwhile, Zn-doped Cu_2O, which has a very low positive formation energy under Cu-poor conditions, has been also fabricated experimentally [14].

Table 3 Formation Energies ΔE_{form}(eV/atom) of M-doped Cu_2O systems

System	ΔE_{form} (eV/atom)	
	Cu-rich	Cu-poor
Cu_2O:Be	-0.008	-0.023
Cu_2O:Mg	-0.014	-0.030
Cu_2O:Ca	-0.032	-0.048
Cu_2O:Sr	-0.024	-0.040
Cu_2O:Zn	0.020	0.005
Cu_2O:Cd	0.028	0.012
Cu_2O:Hg	0.038	0.022
Cu_2O:Al	0.001	-0.016
Cu_2O:Ga	0.012	-0.004
Cu_2O:In	0.015	-0.001

3.2 Charged defect energetics and transition level

The formation energy $\Delta E_{charged}$ of a charged dopant in a material can be formulated as a function of the Fermi level of electrons. In our case, the formation energy of a charged dopant M substituting a Cu atom is obtained using HSE hybrid functional as fellow [34]:

$$\Delta E_{charged} = E_{(Cu_2O:M;q)} - E_{Cu_2O} - \mu_M \\ + \mu_{Cu} + q\left(E_{VBM} + \varepsilon_F\right) + E_{corr} \quad (3)$$

where $E_{(Cu_2O:M;q)}$ and E_{Cu_2O} are the total energies of defect and defect free supercells, respectively. μ_M, and μ_{Cu} are the chemical potentials of the dopant M and Cu, respectively. q is the charge state, which is taken

here as $-2, -1, 0, +1, +2$. E_{VBM} is the energy of the valence band maximum (VBM) of the defect free system, and ε_F is the Fermi level of electrons measured from the VBM. E_{corr} is the correction energy necessary due to periodic interaction between charges in doped systems. Here, we used the scheme proposed by Freysoldt et al. [34]. We calculated the defect energetic considering Cu-poor conditions due to their lower formation energies.

The calculated band gap energy of pure Cu_2O is 2.04 eV, in agreement with the empirical data (2.1 eV [12]). We have calculated the most stable transition level (TL) for each impurity as function of the Fermi energy in the O-rich/Cu-poor conditions. The results are presented in Fig. 2. One can immediately notice the trends for each group. TL of 2A group doped Cu_2O follow an ascending order, where Be and Mg show a TL from charge state $+$ to 0, $\varepsilon(+/0)$ of 0.62 eV, 0.28 eV, respectively, below the conduction band maximum (CBM). Whist, Ca shows TL $\varepsilon(+/0)$ of 0.07 eV above the CBM. Interestingly Sr does not follow this trend and presents two TLs; a relatively deep $\varepsilon(+/0)$ of 0.4 eV below CBM, and another very deep $\varepsilon(2+/+)$ of 0.86 eV. Above VBM. Ca is a shallow donor with $\varepsilon(+/0)$ lying above the CBM, suggesting that Ca impurity as the best candidate among 2A group dopants for n-type conductivity in Cu_2O.

Similar to group 2A, TLs of 12B group impurities follow an ascending order, where Zn, Cd, and Hg have transition levels $\varepsilon(+/0)$ of 0.54 eV, 0.21 eV, and 0.07 eV, below the CBM, respectively. The impurities of interest in this group are Cd and Hg as they present shallow transition levels, and thus act as efficient donor in the metal oxide.

For the 3A group, we notice that the transition levels for Al and In in the charged state $(+2/+)$ are

Fig. 2 Thermodynamic transition levels for M defects in Cu_2O, determined from formation energies. M = Be, Mg, Ca, Sr, Zn, Cd, Hg, Al, Ga, and In
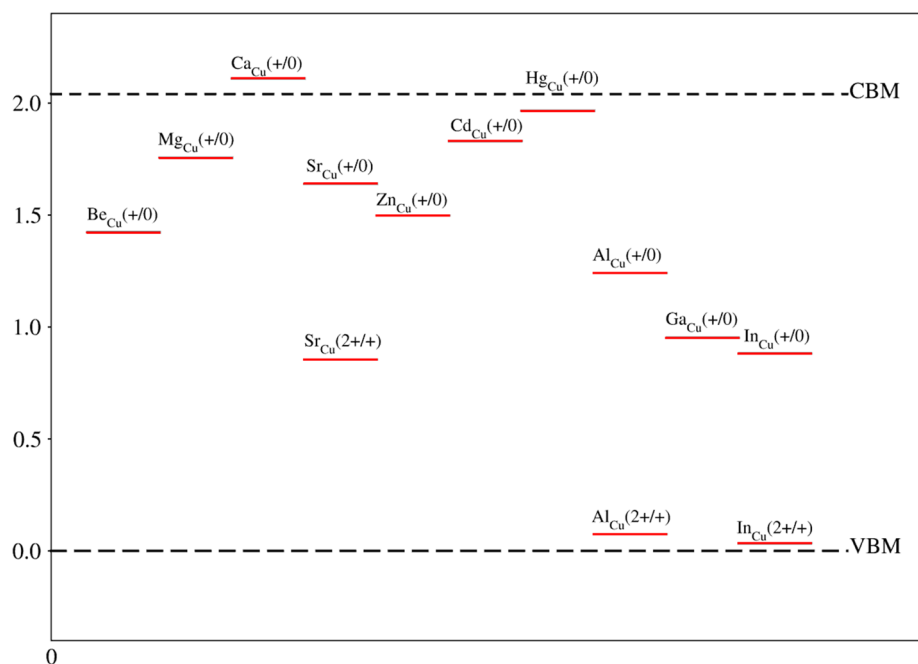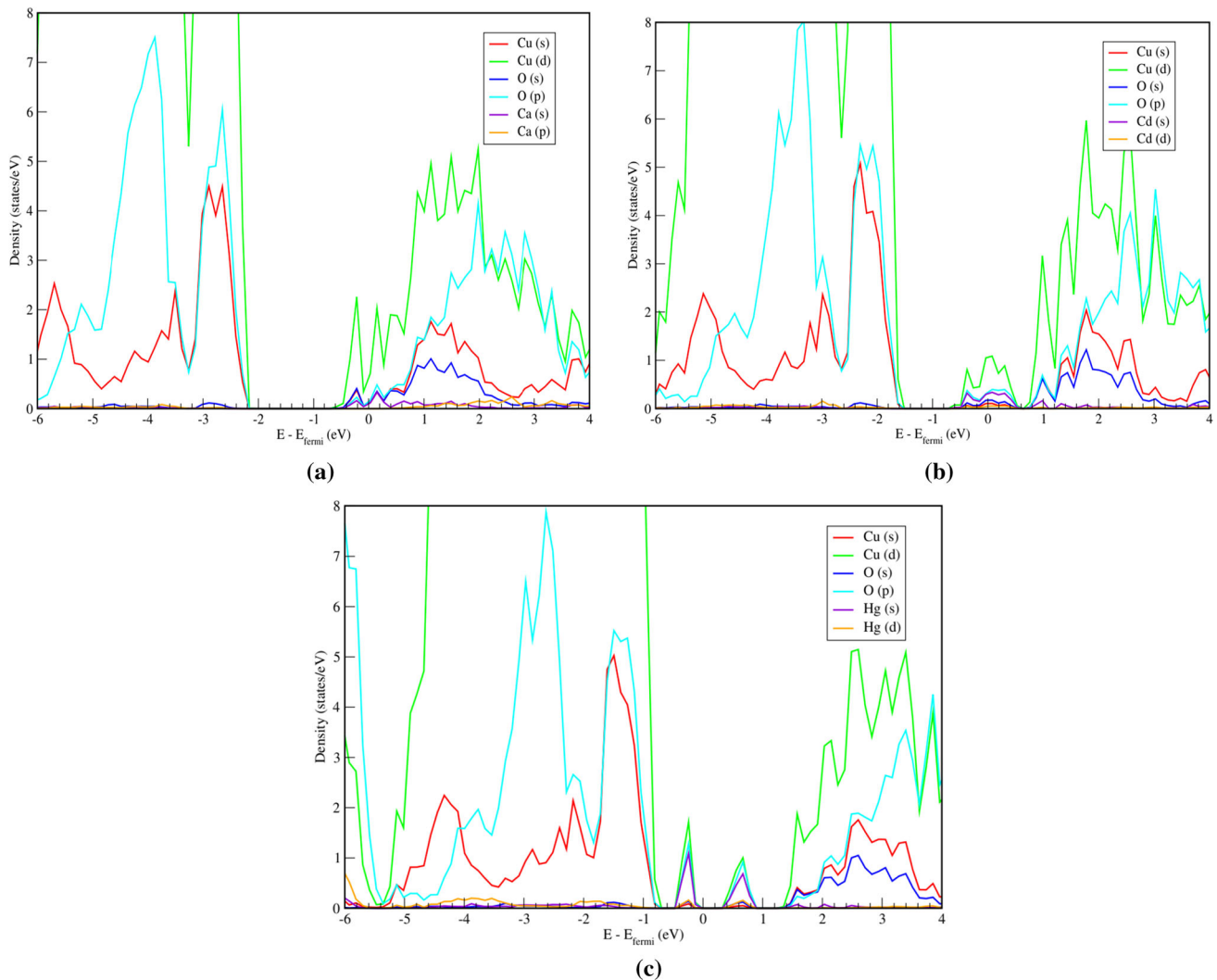
Fig. 3 HSE06 calculated DOS of **a** Ca, **b** Cd and **c** Hg-doped Cu_2O

0.08 eV and 0.04 eV, above the VBM, respectively. These TLs represent ultra-deep donors, severely reducing the intrinsic p-type conductivity of Cu_2O by passivating the TL of V_{Cu}, which were calculated to be at 0.22 eV above the VBM by Scalon et al. [35]. This can explain the improved conductivity found experimentally in In-doped Cu_2O [13]. We can obviously see that Ca, Cd, and Hg dopants are the most promising candidates for n-type conductivity in Cu_2O due to their shallow transition level.

The densities of state (DOS) plots of pure, Ca, Cd and Hg-doped Cu_2O are gathered in Fig. 3a, b and c, respectively. The valence band does not present noticeable change. However, the major change is in the conduction band, where the incorporation of the dopants Cd and Hg leads to the separation of some conduction band states creating, a band in the gap formed by Cu (3d) states with contributions of O (2p) and Cd (5s) states. However, Hg presents two bands in the band gap formed mostly by the hybridization of Cu (3d), O (2p) and Hg (6s) states. This bandgap states can

interact with charge carriers and leads to the recombinations. In contrary, Ca incorporation presents no gap states which means that charge carriers have no obstacles when moving from the valence band to the conduction band. This let us suggest Ca as the best option for n-type conductivity in Cu_2O.

3.3 Work function and surface charge inversion

Surface inversion can be examined through the relative position of the Fermi level of a surface supercell with respect to the vacuum using the work function. The work function, Φ_w, of M-doped Cu_2O surface were calculated and compared to the pure case in order to analyze the surface effects of doped systems, and the type of conductivity induced by the surface inversion, following the formula [13]:

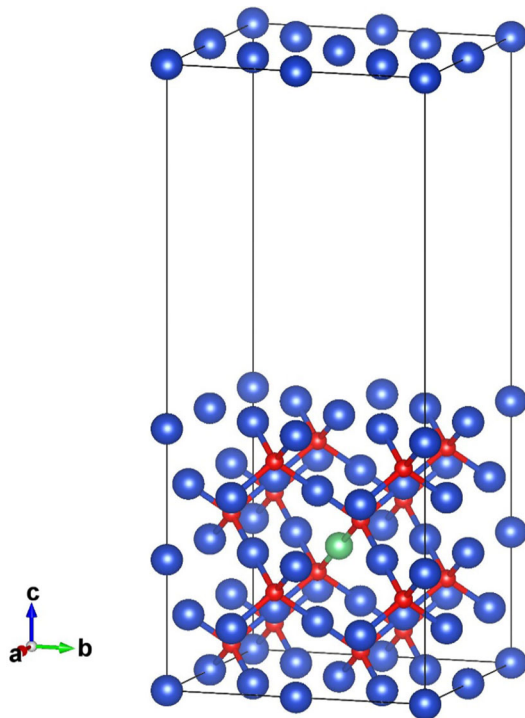$$\Phi_w = \Phi_0 e - E_F \qquad (4)$$

Fig. 4 Surface supercell of M-doped Cu_2O. Blue, red and green spheres represent Cu, O, and M = Be, Mg, Ca, Sr, Zn, Cd, Hg, Al, Ga, and In ions, respectively

Table 4 Calculated work function (in eV) of M-doped Cu_2O systems

System	Φ_w (eV)	System	Φ_w (eV)
Cu_2O:Be	4.181	Cu_2O:Cd	3.846
Cu_2O:Mg	3.901	Cu_2O:Hg	4.010
Cu_2O:Ca	3.813	Cu_2O:Al	3.884
Cu_2O:Sr	3.812	Cu_2O:Ga	4.184
Cu_2O:Zn	3.806	Cu_2O:In	3.815

where Φ_0 is the electrostatic potential of a vacuum level far from the surface, e is the charge of an electron, and E_F is the energy of the Fermi level.

The surface supercell model used for the work function calculation is illustrated in Fig. 4. The electrostatic potential is calculated for the surface, then the vacuum level energy is deduced from the averaged potential along the z direction. While, the Fermi level is extracted from the OUTCAR file. The calculated work functions are summarized in Table 4.

To assess the accuracy of our computation method, we calculated the work function of pure Cu_2O to be 3.894 eV; however, the experimental data of the work function is 4.80 eV [36]. Luckily, we are looking for the relative change in the work function, therefore the accuracy of the results is not very important in this case. From Table 4, we can see that the surfaces of the dopants Be, Mg, Hg, and Ga flip the conductivity from

n-type to p-type due to surface effects. This can explain the results of Jacob et al. [29], where they found a p-type conductivity for Mg-doped Cu_2O. We propose here that this p-type conductivity is due to surface effects and not to the impurity level.

Based on these findings and the previous results of the charge level transition, we propose; Ca and Cd as promising dopants for n-type conductivity in Cu_2O.

3.4 Optical properties

The optical properties at a microscopic level can be described by the complex dielectric response function $\varepsilon(\omega) = \varepsilon_1(\omega) - i\varepsilon_2(\omega)$ in linear response range. The imaginary part ε_2 can be calculated from the momentum matrix elements between the occupied and unoccupied wave functions, then the Kramers–Kronig relation is used to calculate the real part ε_1 from the imaginary part following the equations [37, 38]:

$$\varepsilon_2(\omega) = \left(\frac{4\pi^2 e^2}{m^2\omega^2}\right) \sum_{i,j} \int_k \langle i|M|j\rangle^2 f_i(1-f_i)$$
$$\times \delta(E_{i,j} - E_{i,k} - \omega) d^3k \quad (5)$$

$$\varepsilon_1(\omega) = 1 + \frac{2}{\pi} p \int_0^\infty \frac{\omega'\varepsilon_2(\omega')d\omega'}{(\omega'^2 - \omega^2)} \quad (6)$$

where m, ω and e are the free electron mass, the frequency and the electron charge, respectively. M is the dipole matrix, i and j are the initial and final states, respectively. f_i is the Fermi distribution function for the ith state and E_i is the energy of an electron in the ith state. The specific optical properties of the material can be deduced using ε_1 and ε_2 [39], including absorption coefficient $\alpha(\omega)$, refractive index $n(\omega)$ and reflectivity $R(\omega)$, where:

$$\alpha(\omega) = \sqrt{2}\omega\left[\sqrt{\varepsilon_1^2(\omega) - \varepsilon_2^2(\omega)} - \varepsilon_1(\omega)\right]^{\frac{1}{2}} \quad (7)$$

$$R(\omega) = \left|\frac{\sqrt{\varepsilon(\omega)} - 1}{\sqrt{\varepsilon(\omega)} + 1}\right|^2 \quad (8)$$

To assess the optical properties of the doped systems, optical absorption coefficient and reflectivity were calculated and compared to pure Cu_2O. Figure 5 shows optical properties (absorption coefficient and reflectivity) of the 2A group doped Cu_2O compared to pure case. Trends can be noticed from the figure, there is a great similarity in absorption between 1.5 and 7.0 eV for all elements of the group; suggesting that doping does not change the optical properties above 1.5 eV. It is most noticeable that the dopants Be, Ca and Sr lead to absorption peak around 0.39 eV due to conduction band edge absorption. While, Mg leads to peak around 0.91 eV. The reflectivity plots of 2A dopants are very similar above 1.5 eV. However, the behavior differs below 1.5 eV. Be and Sr reflectivity are very

Fig. 5 Calculated optical properties of group 2A doped Cu_2O compared with the pure Cu_2O case **a** absorption coefficient and **b** reflectivity


(a)

(b)
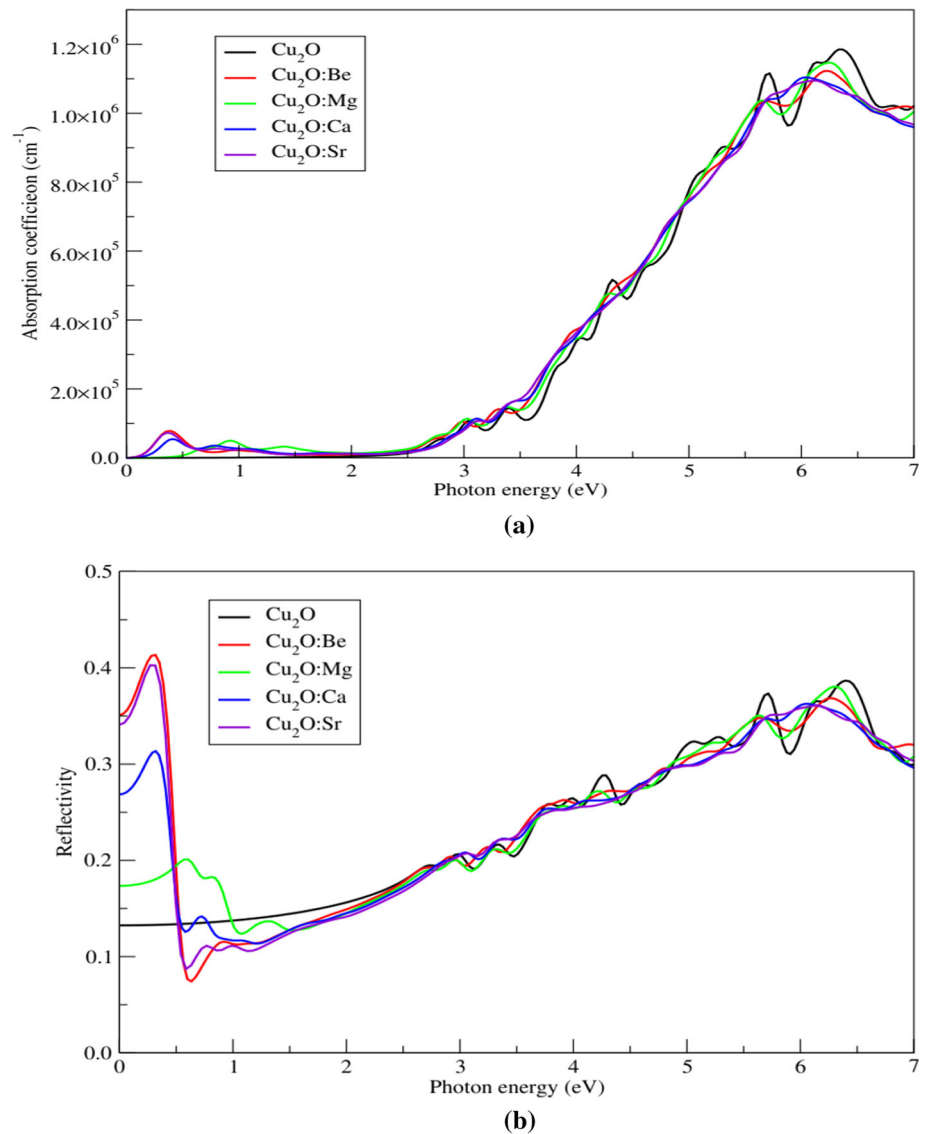
similar with peaks around 0.30 eV with a reflectivity of 0.4 suggesting that these dopants have high reflectivity for infrared photons. Meanwhile, Mg and Ca have peaks around 0.58 eV and 0.31 eV, respectively.

Figure 6 shows the optical properties of 12B doped Cu_2O. There is a clear gain in absorption below 4 eV for all dopants, with Hg having the highest absorption gain. The reflectivity plots of 12B dopants are very similar above 2.7 eV. However, the behavior differs below 2.7 eV. Cd has a peak of 1.63 around 1.8 eV and Zn has a peak of 1.9 around 1.7 eV, showing that it is more reflective in the infrared region. While, Hg reflectivity is similar to the pure case, indicating that it does not reflects in the infrared.

Figure 7 shows the optical properties of 3A doped Cu_2O. All dopants result in a remarkable increased absorption between 1 and 4 eV. Al doping leads to absorption in the range (1–2) eV, indicating an intermediate band gap material. Intermediate-band photovoltaics open a new way of surpassing the performance limits of Shockley-Queisser in solar cells. It introduces an intermediate band (IB) energy level between the valence and conduction bands. In theory, the introduction of an IB permits two photons of less energy than the band gap to energize an electron from the valence band to the conduction band, thus increasing the induced photo-current and consequently improving efficiency. Ga and In have similar effects on the absorption coefficient, where both ions lead to an important absorption around (2–3) eV due to conduction band edge absorption. Al dopant shows high reflectivity between 1.4 and 1.8 eV with a peak of 0.24. While, Ga and In dopants show similar trends peaking at 2.5 eV.

Fig. 6 Calculated optical properties of group 12B doped Cu_2O compared with the pure Cu_2O case **a** absorption coefficient and **b** reflectivity


(a)

(b)
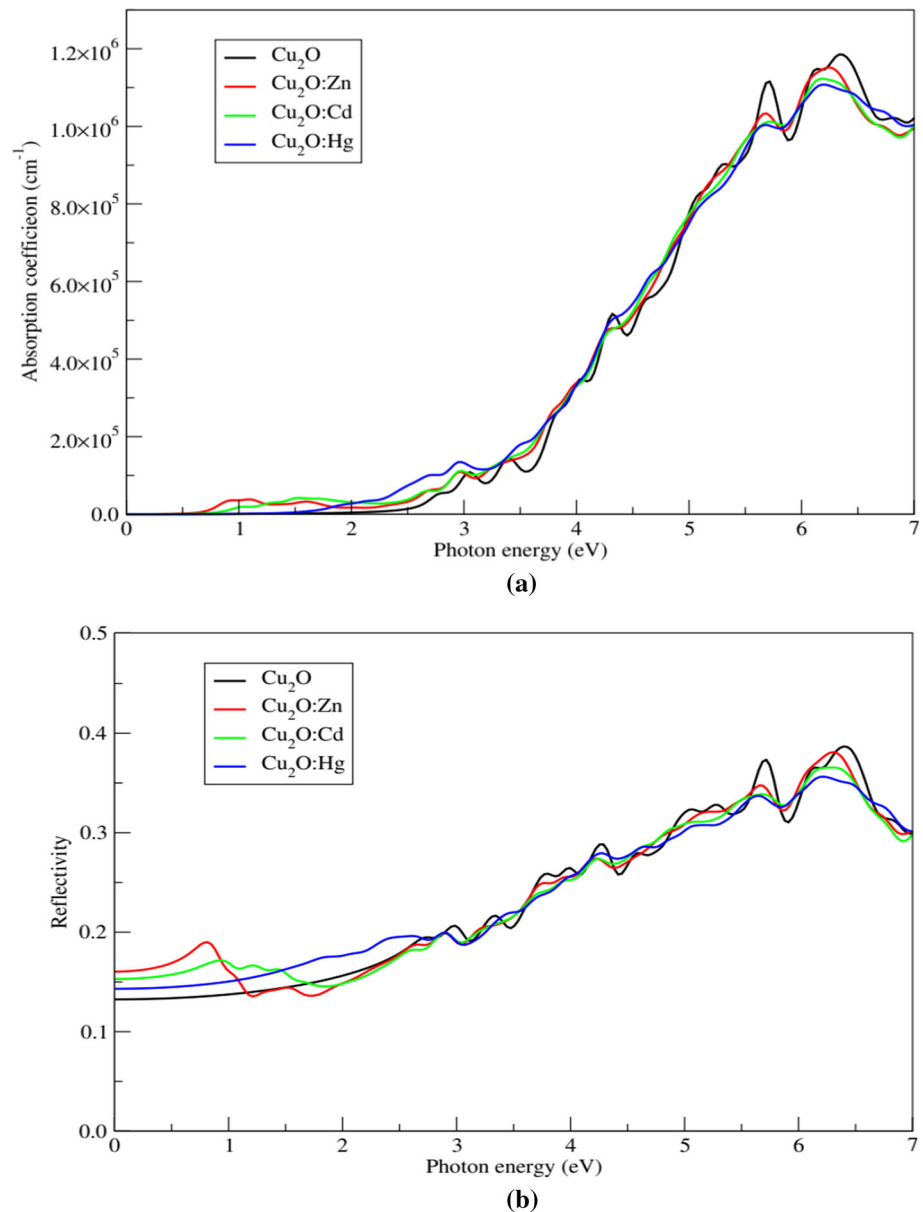
4 Conclusion

Structural, energetic, electronic and optical analyses of M (M = Be, Mg, Ca, Sr, Zn, Cd, Hg, Al, Ga, and In)-doped Cu_2O were performed under periodic boundary conditions using DFT based on plane waves methodologies. The model doping concentration is about 3.12% to agree well with experimental concentrations. The calculated structural parameters show that Be dopant have compression effects on the system, reducing the lattice parameter 'a' by 0.13%. On the other hand, Mg, Ca, Sr, Zn, Cd, Hg, Al, Ga and In have expansion effects, with increasing of 'a' by 0.48% and 0.93%, 1.23%, 0.42%, 0.81%, 0.87%, 0.45%, 0.52%, and 0.94%, respectively. The crystal distortion caused by doping is very small for all systems, signifying that these systems could still preserve the Cu_2O original crystal structure.

Analyzing the solubility of the dopants in the Cu_2O matrix based on the formation energy for Cu-rich and Cu-poor conditions, we were able to show that group 2A elements (Be, Mg, Ca, Sr) are stable under both conditions. While, the incorporation of group 12B (Zn, Cd, Hg) is energetically unfavorable under both conditions due to their positive formation energy. Meanwhile, 3A group impurities (Al, Ga, In) could be readily incorporated into the crystal lattice of Cu_2O under Cu-poor conditions.

For group 2A dopants, the charge transition levels follow an ascending order, with Ca showing the shallowest TL. Similar to 2A group, TLs of 12B group impurities follow an ascending order, where Cd and Hg present the shallowest transition level. For the 3A group, we found the TLs of Al and In dopants are located ultra-deep in

Fig. 7 Calculated optical properties of group 3A doped Cu$_2$O compared with the pure Cu$_2$O case **a** absorption coefficient and **b** reflectivity

(a)

(b)
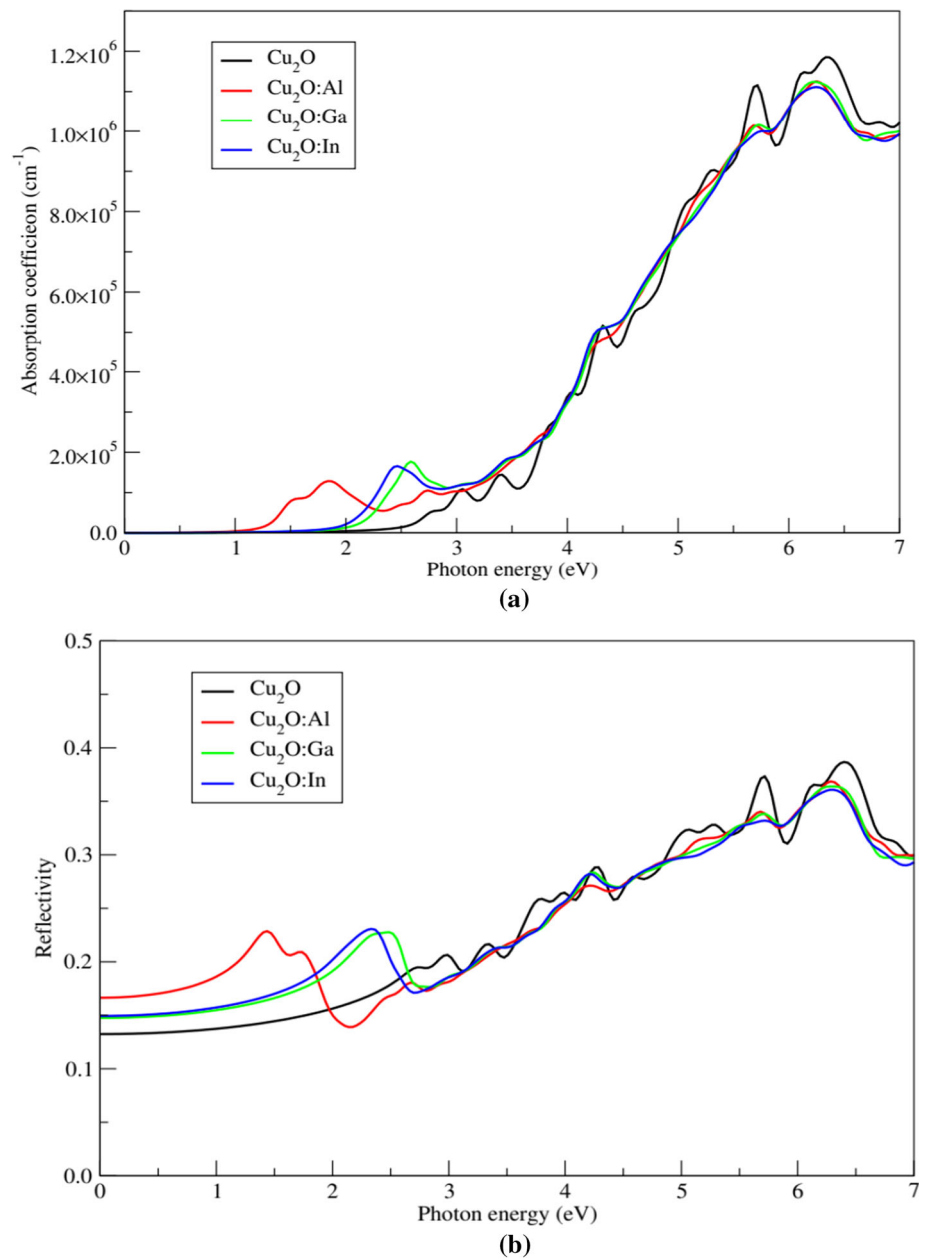
the band gap, severely reducing the intrinsic p-type conductivity of Cu$_2$O by passivating the TL of V$_{Cu}$. The calculated work functions indicate that the surfaces of the dopants Be, Mg, Hg, and Ga flip the conductivity from n-type to p-type due to surface effects.

The optical properties of group 2A doped Cu$_2$O show great similarity in absorption between 1.5 and 7.0 eV, suggesting that doping does not change the optical properties in this region. For group 12B doped Cu$_2$O, there is a clear gain in absorption below 4 eV for all dopants, with Hg having the highest absorption gain. For the optical properties of group 3A doped Cu$_2$O, all dopants result in a remarkable increased absorption between 1 and 4 eV, with Al doping leading to absorption in the range (1–2) eV; indicating an intermediate band gap material.

The results found here favor Ca doping as the most promising to induce n-type conductivity, and Al doping for most promising optical performance in Cu$_2$O.

Author contributions

MB: conceptualization, methodology, software, validation, formal analysis, investigation, resources, writing and original draft preparation, visualization. HSA: visualization, validation, writing, review and editing. GM: conceptualization, validation, supervision, project administration.

Declarations

Conflict of interest The authors declare that they have no conflicts of interest.

References

1. L.C. Andreani, A. Bozzola, P. Kowalczewski, M. Liscidini, L. Redorici, Silicon solar cells: toward the efficiency limits. Adv. Phys. X **4**, 1548305 (2019)
2. P.K. Nayak, S. Mahesh, H.J. Snaith, D. Cahen, Photovoltaic solar cell technologies: analysing the state of the art. Nat. Rev. Mater. **4**, 269–285 (2019)
3. M.M. Moharam, E.M. Elsayed, J.C. Nino, R.M. Abou-Shahba, M.M. Rashad, Potentiostatic deposition of Cu2O films as p-type transparent conductors at room temperature. Thin Solid Films **616**, 760–766 (2016)
4. A. Rakshit, K. Islam, R. Sultana, S. Chakraborty, Effect of oxygen content and crystallization temperature on the insulator-to-metal transition properties of vanadium oxide thin-films. Vacuum **180**, 109633 (2020)
5. F. He, X. Yin, J. Li, S. Lin, L. Wu, X. Hao, J. Zhang, L. Feng, Characterization of sputtered MoOx thin films with different oxygen content and their application as back contact in CdTe solar cells. Vacuum **176**, 109337 (2020)
6. S. Li, Z. Shi, Z. Tang, X. Li, Comparison of ITO, In 2 O 3: Zn and In 2 O 3: H transparent conductive oxides as front electrodes for silicon heterojunction solar cell applications. Vacuum **145**, 262–267 (2017)
7. S.S. Sunu, E. Prabhu, V. Jayaraman, K.I. Gnanasekar, T. Gnanasekaran, Gas sensing properties of PLD made MoO3 films *Sens*. Actuators B Chem. **94**, 189–196 (2003)
8. S.J. Mezher, M.O. Dawood, O.M. Abdulmunem, M.K. Mejbel, Copper doped nickel oxide gas sensor. Vacuum **172**, 109074 (2020)
9. M.-J. Hong, Y.-C. Lin, L.-C. Chao, P.-H. Lin, B.-R. Huang, Cupric and cuprous oxide by reactive ion beam sputter deposition and the photosensing properties of cupric oxide metal–semiconductor–metal Schottky photodiodes. Appl. Surf. Sci. **346**, 18–23 (2015)
10. X. Han, K. Han, M. Tao, n-Type Cu2O by electrochemical doping with Cl. Electrochem. Solid-State Lett. **12**, H89 (2009)
11. S. Dolai, S. Das, S. Hussain, R. Bhar, A.K. Pal, Cuprous oxide (Cu2O) thin films prepared by reactive d.c. sputtering technique. Vacuum **141**, 296–306 (2017)
12. A.A. Ejigu, L. Chao, Characterization of n-type Cu2O deposited by reactive ion beam sputter deposition. J. Vac. Sci. Technol. B Nanotechnol. Microelectron. Mater. Process. Meas. Phenom. **35**, 061205 (2017)
13. X.-M. Cai, X.-Q. Su, F. Ye, H. Wang, X.-Q. Tian, D.-P. Zhang, P. Fan, J.-T. Luo, Z.-H. Zheng, G.-X. Liang, V.A.L. Roy, The n-type conduction of indium-doped Cu 2 O thin films fabricated by direct current magnetron co-sputtering. Appl. Phys. Lett. **107**, 083901 (2015)
14. C. Zhu, M.J. Panzer, Synthesis of Zn: Cu 2 O thin films using a single step electrodeposition for photovoltaic applications. ACS Appl. Mater. Interfaces **7**, 5624–5628 (2015)
15. C.M. McShane, K.-S. Choi, Junction studies on electrochemically fabricated p–n Cu2O homojunction solar cells for efficiency enhancement. Phys. Chem. Chem. Phys. **14**, 6112 (2012)
16. Y.-K. Hsu, J.-R. Wu, M.-H. Chen, Y.-C. Chen, Y.-G. Lin, Fabrication of homojunction Cu2O solar cells by electrochemical deposition. Appl. Surf. Sci. **354**, 8–13 (2015)
17. M. Sieberer, J. Redinger, P. Mohn, Electronic and magnetic structure of cuprous oxide Cu2O doped with Mn, Fe Co, and Ni: a density-functional theory study. Phys. Rev. B **75**, 035203 (2007)
18. M. Benaissa, H. Si Abdelkader, G. Merad, Electronic and optical properties of halogen (H= F, Cl, Br)-doped Cu2O by hybrid density functional simulations. Optik **207**, 164440 (2020)
19. P.E. Blöchl, Projector augmented-wave method. Phys. Rev. B **50**, 17953–17979 (1994)
20. J. Heyd, G.E. Scuseria, M. Ernzerhof, Hybrid functionals based on a screened Coulomb potential. J. Chem. Phys. **118**, 8207–8215 (2003)
21. P. Hohenberg, W. Kohn, Inhomogeneous electron gas. Phys. Rev. **136**, B864–B871 (1964)
22. W. Kohn, L.J. Sham, Quantum density oscillations in an inhomogeneous electron gas. Phys. Rev. **137**, A1697–A1705 (1965)
23. D.O. Scanlon, G.W. Watson, Uncovering the complex behavior of hydrogen in Cu2O. Phys. Rev. Lett. **106**, 186403 (2011)
24. G. Kresse, J. Hafner, Ab initio molecular dynamics for liquid metals. Phys. Rev. B **47**, 558–561 (1993)
25. G. Kresse, J. Furthmüller, Efficient iterative schemes for ab initio total-energy calculations using a plane-wave basis set. Phys. Rev. B **54**, 11169–11186 (1996)
26. H.J. Monkhorst, J.D. Pack, Special points for Brillouin-zone integrations. Phys. Rev. B **13**, 5188–5192 (1976)
27. J. Zemann, Crystal structures, 2nd edition. Vol. 1 by R. W. G. Wyckoff. Acta Crystallogr. **18**, 139–139 (1965)
28. Biccari F (2012) Defects and doping in Cu2O. Lulu Com
29. S.S.K. Jacob, I. Kulandaisamy, S. Valanarasu, A.M.S. Arulanantham, V. Ganesh, S. AlFaify, A. Kathalingam, Enhanced optoelectronic properties of Mg doped Cu2O thin films prepared by nebulizer pyrolysis technique. J. Mater. Sci. Mater. Electron. **30**, 10532–10542 (2019)
30. S. Mihai, A. Mihai, M.C.-M. Jose, N. Madalina, O. Petre, P. Silviu, C. Maria, M. Mircea, G. Mariuca, Sr doped Cu2O a new p-type material for photovoltaic applications. Rev Roum Chim **63**, 425–435 (2018)

31. K. Matsunaga, T. Tanaka, T. Yamamoto, Y. Ikuhara, First-principles calculations of intrinsic defects in Al2O3. Phys. Rev. B **68**, 085110 (2003)

32. J.K. Burdett, T. Hughbanks, G.J. Miller, J.W. Richardson, J.V. Smith, Structural-electronic relationships in inorganic solids: powder neutron diffraction studies of the rutile and anatase polymorphs of titanium dioxide at 15 and 295 K. J. Am. Chem. Soc. **109**, 3639–3646 (1987)

33. L.Y. Isseroff, E.A. Carter, Electronic structure of pure and doped cuprous oxide with copper vacancies: suppression of trap states. Chem. Mater. **25**, 253–265 (2013)

34. C. Freysoldt, B. Grabowski, T. Hickel, J. Neugebauer, G. Kresse, A. Janotti, C.G. Van de Walle, First-principles calculations for point defects in solids. Rev. Mod. Phys. **86**, 253–305 (2014)

35. D.O. Scanlon, G.W. Watson, Uncovering the Complex Behavior of Hydrogen in Cu 2 O. Phys. Rev. Lett. **106**, 186403 (2011)

36. C.-S. Tan, S.-C. Hsu, W.-H. Ke, L.-J. Chen, M.H. Huang, Facet-dependent electrical conductivity properties of Cu 2 O crystals. Nano Lett. **15**, 2155–2160 (2015)

37. Y. Jiang, H. Yuan, H. Chen, Enhanced visible light photocatalytic activity of Cu 2 O via cationic–anionic passivated codoping. Phys. Chem. Chem. Phys. **17**, 630–637 (2015)

38. M. Gajdoš, K. Hummer, G. Kresse, J. Furthmüller, F. Bechstedt, Linear optical properties in the projector-augmented wave methodology. Phys. Rev. B **73**, 045112 (2006)

39. V. Wang, N. Xu, J.C. Liu, G. Tang, W.-T. Geng, VASPKIT: a user-friendly interface facilitating high-throughput computing and analysis using VASP code (2019)